

***In situ* grazing-incidence x-ray-diffraction and electron-microscopic studies of small gold clusters**

Kenji Koga and Harutoshi Takeo

National Institute for Advanced Interdisciplinary Research, 1-1-4 Higashi, Tsukuba, Ibaraki 305, Japan

Takuji Ikeda and Ken-ichi Ohshima

Institute of Applied Physics, University of Tsukuba, Tsukuba, Ibaraki 305, Japan

(Received 14 April 1997; revised manuscript received 21 August 1997)

Small gold clusters having diameters of 1–3 nm have been studied by using x-ray-diffraction and electron microscopy. Large amounts of small gold clusters generated by the inert-gas vapor-condensation method were deposited on a silicon wafer cooled down to 92 K to avoid coalescence growth and grazing-incidence x-ray-diffraction intensity from the cold cluster deposit was measured *in situ*. The diffraction pattern was analyzed and compared quantitatively with calculated patterns from several structural models considering the observed size distribution and found to be explainable approximately by a decahedral structure with geometrically closed shells. Electron-microscopic observations for gold clusters deposited sparsely on an amorphous carbon film at room temperature were also performed and decahedral multiply-twinned clusters 2–3 nm in diameter were frequently observed. This result agrees well with the x-ray statistical result, suggesting that the most dominant structure of small gold clusters prepared under our experimental conditions is the decahedral structure. The present experiments have demonstrated that an extremely weak x-ray-diffraction signal from such a small cluster can be measured quantitatively by preparing a cold cluster deposit. [S0163-1829(98)02408-4]

I. INTRODUCTION

Characterization of the unique structures of clusters prepared from inorganic or metallic matters is of great importance to understand the crystal growth nature and also the physical and chemical properties of clusters. Direct observation of atomic arrangements in clusters can be achieved by means of high-resolution transmission-electron microscopy (HRTEM). Icosahedral and decahedral gold clusters with fivefold symmetry axes have been discovered in initially grown islands prepared by the vapor deposition on a cleaved surface of ionic crystals.^{1,2} On the other hand, statistical information on the structure of clusters can be provided conveniently by using the electron-diffraction (ED) experiment. Over the past decade, the ED method has been applied directly to supersonic expansion beams of metal clusters,^{3–5} since the electron beam shows a very strong interaction with atoms. However the quantitative analysis of ED patterns from metal clusters cannot be treated in a simple way, because of the dynamical effects due to multiple scattering of the electron beam in the matter. Gold clusters of only 1.6 nm in diameter gave rise to the effects in diffraction intensities exceeding 25%,⁶ and the kinematic theory (Born approximation) fails completely for lower angle reflections from crystalline clusters.^{7,8}

Quantitative determinations of crystal structures have been performed very conveniently by means of the x-ray-diffraction (XRD) method, since intensities can be treated perfectly by the kinematic theory. A great number of works have been carried out by recording Debye-Scherrer diffraction rings from powder or polycrystalline samples using the Debye-Scherrer camera or the powder diffractometer. However, until now there have been only a few cases where this technique has been utilized for clusters, because accumulation of many clusters is necessary to obtain the diffraction

intensity with a sufficient signal-to-noise ratio. Furthermore a narrow size distribution of clusters is required to accomplish a quantitative analysis. When one collects many clusters on a solid substrate at room temperature, small clusters hardly pile up, keeping their initial conformations and interior structures due to the spontaneous coalescence among them. This problem in treating many small clusters, e.g., gold clusters smaller than 5 nm in diameter, has already been pointed out previously.⁹ Matrix-isolation techniques have been used to collect many small clusters, keeping their initial conformation. The influence of the matrix on the structure of metal clusters might be neglected in the case that they are surrounded by a soft matrix matter formed with van der Waals bonds. Recently extended x-ray-absorption fine-structure (EXAFS) measurements have been carried out for gold clusters isolated in a Mylar film, silver clusters in solid argon, etc.^{10,11} With XRD experiments, however, it will be difficult to obtain data reliable enough to be analyzed quantitatively, because the broad patterns from the clusters are considerably perturbed by the intense Bragg reflections from the solid matrices.

The XRD experiments for the clusters requires a cluster assemblage, in which each cluster is stacked and connected, weakly retaining its original shape and structure. We have expected that such a sample can be produced by cluster deposition on a solid substrate cooled down to low temperature, e.g., liquid-nitrogen temperature, where clusters are so rapidly quenched that they do not coalesce with each other. We call this procedure low-temperature cluster deposition (LTCD). In this paper, we introduce a preparation of a gold cluster deposit on a cold substrate and an *in situ* XRD measurement for this deposit. The present experiment has provided statistical and quantitative information on the structure of small gold clusters.

II. EXPERIMENTAL AND RESULTS

A. Apparatus

To perform the LTCD and the *in situ* XRD measurement, we have combined an XRD device with cluster formation and deposition chambers. The details of the apparatus are described in the previous paper.¹² Cluster formation is carried out by the vapor condensation method using helium gas. In the formation chamber, vapor is produced from material in a graphite crucible heated with induction coils. Clusters generated in the inner zone¹³ are selected with a skimmer and carried with a helium gas stream into the deposition chamber through a nozzle, which is evacuated by a mechanical booster pump. Residual clusters generated in the outer zone and the inner front¹³ are evacuated by a rotary pump through a tube concentric with the nozzle. The substrate in the deposition chamber is thermally connected to a liquid-nitrogen cryostat. Clusters spouting out of the nozzle are deposited on the cooled substrate. After deposition, the substrate is moved to a rotation center of an x-ray diffractometer by changing the cryostat position while keeping both the vacuum and the temperature conditions. The grazing-incidence x-ray-diffraction (GIXRD) method was employed to obtain a weak signal from clusters. A line-focus x-ray beam generated from a Cu anode irradiates to the substrate surface with a fixed grazing-incidence angle of 2° through a vacuum-tight carbon-fiber window. The diffracted beam passes through a soller slit and the Cu $K\alpha$ characteristic line is selected by a highly oriented pyrolytic graphite (HOPG) monochromator crystal. Then the beam is detected by a scintillation counter.

B. Quantitative inspection of the GIXRD system

The GIXRD method is widely used to measure diffracted intensities from thin films. By setting a small incidence angle, the path length of the x rays in a thin film can be increased and a large irradiated area can be covered with the help of a line-focus incident beam, resulting in a considerable improvement of the signal-to-noise ratio. There have been many measurements using this technique, however the diffraction intensity has not been treated quantitatively in most cases because the effective area of the monochromator usually does not cover the diffracted beam in the whole 2θ range. The horizontal width of the diffracted beam changes with the scattering angle 2θ by $L_{IA} \sin(2\theta - \alpha)$, where L_{IA} is the horizontal length of the irradiated area of the substrate surface, and α is the angle of incidence (2°). The width of the diffracted beam at the sample position reaches a maximum ($=L_{IA}$) at $2\theta = 90^\circ + \alpha$. The irradiated area on the substrate was estimated to be 9 (h) \times 12 (v) mm^2 , which was obtained from an area of the color center produced by x-ray irradiation on a NaCl powder sample placed instead of the substrate. Therefore, the monochromator should have enough horizontal and vertical width to reflect such a widened beam perfectly.

We employed a flat HOPG monochromator with a large effective area, 50 (h) \times 25 (v) mm^2 , which is enough to cover the maximum area of the diffracted beam at the monochromatic condition of the Cu $K\alpha$ line for the graphite (00-2) reflection. Under the condition in which the whole beam can be detected, the integrated intensities caused by the

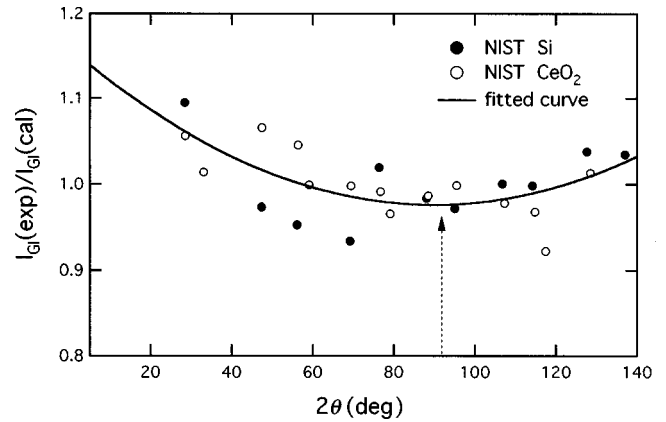


FIG. 1. Closed and open circles indicate the ratios of the experimental integrated intensities to the calculated ones for Si and CeO_2 , respectively, where the experimental data sets were obtained from NIST standard powder samples using the present GIXRD system. An average value of the ratios was normalized into unity for each data set. A solid curve was produced by the least-square fitting the whole data set with a cubic function. It shows a minimum around at $2\theta = 90^\circ + \alpha$, indicated by an arrow, where the diffracted beam becomes maximally wide. This instrumental function was used to correct the diffraction intensities measured by the present GIXRD system.

grazing incidence (GI) geometry, I_{GI} , are directly related to those caused by the Bragg-Brentano (BB) geometry, I_{BB} , with an angular-dependent absorption factor, which can be written in first approximation as follows:

$$I_{GI} = K \frac{2 \sin(2\theta - \alpha)}{\sin \alpha + \sin(2\theta - \alpha)} \zeta(2\theta, \rho t) I_{BB}, \quad (1)$$

$$\zeta(2\theta, \rho t) = 1 - \exp \left[- \left(\frac{\mu}{\rho} \right) \rho t \left(\frac{1}{\sin \alpha} + \frac{1}{\sin(2\theta - \alpha)} \right) \right], \quad (2)$$

where μ is the linear absorption coefficient, t the average thickness, (μ/ρ) the mass absorption coefficient, ρ the density, K a constant coefficient, and I_{BB} the integrated intensity from the same sample with an infinite thickness under the BB geometry. The term $\zeta(2\theta, \rho t)$ becomes unity for the bulk powder sample with $t \gg 1/\mu$. Calculated integrated intensities I_{BB} can be derived using the x-ray scattering form factors¹⁴ based on self-consistent-field calculations.

To check the present GIXRD system, we have measured diffraction patterns from the Si and CeO_2 standard powders (NIST SRM 640b and SRM 674a). The lattice parameter of Si was calculated to be 5.4325 Å using the Cohen method, which agreed well with the literature value 5.4309 Å. The angular-dependent resolution, i.e., the full width at half maximum (FWHM) of the Cu $K\alpha_1$ component was better than 0.3° in the measured range. The correction for this instrumental broadening to the measured diffraction pattern from small gold clusters was not necessary because of the fairly broadened halo pattern. The ratios of measured integrated intensities $I_{GI}(\text{exp})$ to calculated ones $I_{GI}(\text{cal})$ are plotted in Fig. 1, where an average value of the ratios is normalized to unity for each data set. An empirical function drawn with a solid line was produced by least-square-fitting

a cubic function to the whole data set. The function decreased slightly with increasing 2θ up to around 90° and increased again for further increase of 2θ . This tendency can be explained as follows: because the diffracted beam widens with increasing 2θ up to $92^\circ (=90^\circ + \alpha)$, the soller slit might not restrict the beam with a constant ratio, and the counting efficiency might decrease when the beam moves away from the center of the detector window. The experimental intensities can be corrected using this instrumental correction function.

C. Generation of gold clusters

In order to generate small gold clusters with large flux, it was necessary to optimize the following parameters: the crucible temperature (T), the pressures in the formation and deposition chamber (P_F and P_D), and the distance (D) between the skimmer and the crucible. Gold clusters were deposited on a thin amorphous carbon film (commercially available microgrid carbon) at room temperature for a short time. They were well dispersed and did not coalesce with each other. The average size was measured by observing their real images with a conventional TEM, where JEOL JEM-100CXII was employed. By iterating these procedures, we could find a suitable condition to generate gold clusters with a small average size and a flux sufficient to prepare large amounts of deposit for the XRD measurement. The experimental parameters optimized for the generation of small gold clusters were $T=1350^\circ\text{C}$, $P_F=27\text{ hPa}$, $P_D=7\text{ hPa}$, and $D=15\text{ mm}$. The size distribution was derived from TEM pictures using an image-analysis software after loading them into a personal computer through an image scanner. Figure 2(a) shows the size distribution of about 700 gold clusters. The population of clusters smaller than about 0.5 nm in diameter could not be determined due to the resolution limit and the strong substrate image. The distribution is well represented with the log-normal function, as plotted with a solid line in Fig. 2(a). This means that the growth mechanism is mainly governed by coalescence among clusters. From this curve, the average diameter of clusters and the FWHM of the distribution were determined to be 1.36 and 1.16 nm, respectively. The geometrical standard deviation (σ) was 1.51, which falls in a range reported previously.¹⁵

The product of the population of clusters at a given diameter $N(R)$ and the cube of the given diameter R^3 is plotted in Fig. 2(b). Both, the average diameter and the FWHM of this distribution were around 2 nm. The XRD intensity is proportional to this volume-weighted size distribution and not to the observed size distribution shown in Fig. 2(a). Thus, most of the XRD intensity is reflected from clusters with diameters of 1–3 nm.

D. HRTEM observation of gold clusters

Prior to the XRD study, we have performed HRTEM observations to see what type of structure is dominant in gold clusters with 1–3 nm in diameter. Gold clusters were deposited on the amorphous carbon substrate at room temperature under the condition described above. The sample was transferred to the HRTEM in the normal atmosphere. The electron beam was perpendicular to the substrate surface. Elec-

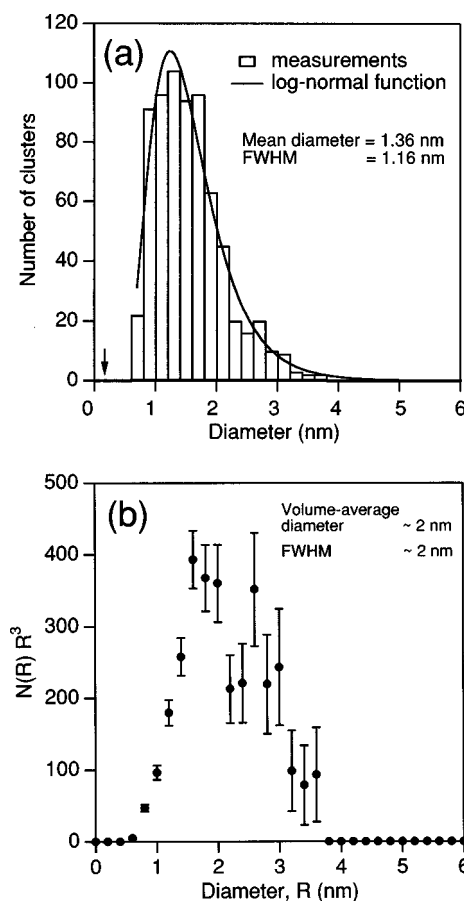


FIG. 2. (a) The size distribution derived directly from TEM photographs of gold clusters with an image-analysis technique. An arrow indicates the resolution limit of the TEM. A solid line was produced by fitting a log-normal function to the data points above 0.6 nm. The average diameter and the FWHM value of the distribution were 1.36 and 1.16 nm, respectively. The geometrical standard deviation σ was 1.51. (b) The volume-weighted size distribution generated by plotting the product of the population $N(R)$ and R^3 , where R is the diameter. Both, the average diameter and the FWHM value were about 2 nm. The XRD intensity is reflected from this distribution (mostly 1–3 nm) instead of the size distribution in (a).

tron micrographs have been taken with a magnification of 8×10^5 and about 100 clusters were examined, using JEOL JEM-2010 with a point resolution of 0.194 nm. We could see that clusters having 2–3 nm in diameter frequently exhibited decahedral multiply-twinned structures. Figure 3(a) shows an image of a five-shelled decahedral gold cluster with about 2.5 nm in diameter, which has a fivefold axis nearly parallel to the beam direction. The five corners of the pentagon showed no clear indication of facets. A smaller cluster shown in Fig. 3(b) is a four-shelled decahedron tilting slightly from the beam direction. This also looks like a regular decahedron without facets. Instead of these images exhibiting five tetrahedral segments clearly, most of the clusters showed complex images due to tilting of the fivefold axis. Two clusters with larger tilting angles are shown in Figs. 3(c) and 3(d). These two clusters are five-shelled regular decahedra without any clear facet. The tilting angle of the cluster shown in Fig. 3(c) was estimated roughly to be about 20° by comparing with multislice calculation results for tilt series of a gold decahedron,¹⁶ and the cluster in Fig. 3(d) was tilted in the

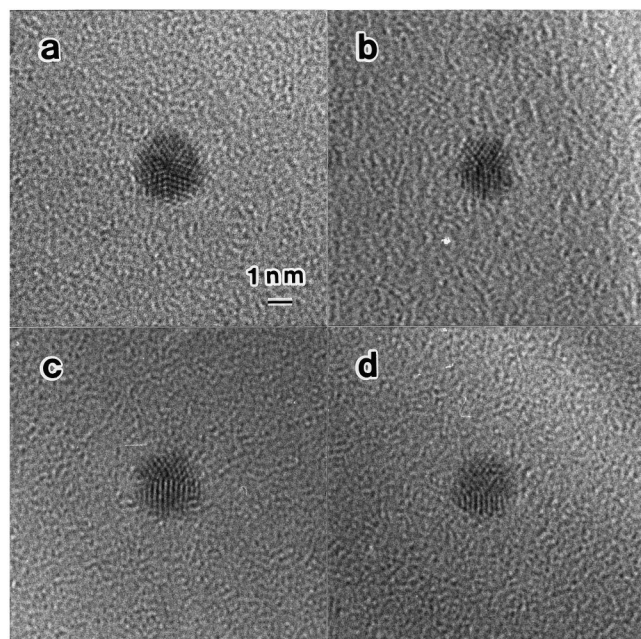


FIG. 3. HRTEM images of gold clusters deposited on an amorphous carbon film. (a) Five-shelled decahedron with a diameter of about 2.5 nm located with its fivefold axis nearly parallel to the beam direction. (b) Four-shelled decahedron with a diameter of about 2 nm slightly tilted upwards. (c) Five-shelled decahedron with an upward tilt of about 20° compared to (a). (d) Five-shelled decahedron with a downward tilt opposite to (c).

opposite direction. When one tetrahedral face of a decahedron is placed parallel to the substrate surface, the tilting angle is 35.8° . Such a large tilting gives rise to fairly distorted and complex images with ellipsoidal outer shapes. We could not find clusters tilted that much, indicating that most of the decahedral clusters were located with their fivefold axis tilting with a few ten degrees from the electron-beam direction.

The HRTEM images we have observed here did not show any patterns expected from the icosahedral multiply-twinned structure, as can be seen by comparing the multislice-calculation images for the icosahedral structure along two-fold, threefold, and fivefold axes.¹⁶ Face-centered-cubic clusters with a single domain or twins have been found occasionally. Some clusters showed complex structures. Structures of gold clusters smaller than 2 nm could not be identified, because they often showed dynamic structural fluctuations like amoebas as Iijima and Ichihashi¹⁷ have observed. The dynamic fluctuation is considered to be of an intrinsic nature due to the quasimelting state at room temperature, however the effect of the electron-beam irradiation on this phenomenon is not yet clear.^{18,19} Strong background images of the amorphous carbon have also prevented us from resolving atomic arrangements.

To recapitulate, gold clusters having 2–3 nm diameter showed dominantly decahedral structures. The structure of clusters smaller than 2 nm in diameter, could not be identified due to both the dynamic structural fluctuation and the strong background image of the substrate. To reveal the most probable structure of gold clusters with 1–3 nm in diameter

much more reliably with the help of statistics, the following x-ray quantitative measurement for cooled clusters was necessary.

E. *In situ* GIXRD measurements of gold clusters deposited on a cooled substrate

LTCD and *in situ* GIXRD measurements were carried out for gold clusters that were generated under the same conditions as in the size-distribution measurement as described in the previous section. A silicon wafer with a dimension of $40\text{ (h)} \times 25\text{ (v)} \times 0.5\text{ (t)}\text{ mm}^3$, whose surface normal is parallel to the [001] direction, was employed as the substrate. It was etched to remove oxidized layers by using a 3% hydrofluoric acid prior to the experiment. A nonreflective crystallographic direction of the substrate for GIXRD measurements was empirically determined, i.e., the [100] direction was inclined 20° from the scattering plane. No tail of Bragg reflections from the silicon single crystal were found in the background intensity measured at 82 K before the deposition. Gold clusters were deposited on the cooled substrate for 1 h. The temperature of the substrate increased up to 92 K due to the helium gas stream. The area where x-ray beam irradiated was covered homogeneously with the clusters. Subsequently, the GIXRD measurement was performed at 82 K. Diffraction data was collected with 2θ ranging from 5° to 130° and a step of 0.1° . A measuring time of 3 s per a step was used and the x-ray generator was operated at 50 kV and 300 mA. Diffraction patterns of the background and the signal, measured in this way, are drawn with thin and thick lines as shown in Fig. 4(a), respectively. A pattern where the background was subtracted from the signal, is drawn with a thick line in Fig. 4(b). Furthermore, the following additional experiment was done to estimate the contribution to the signal intensity caused by contaminating molecules (mainly CO_2) adsorbed on the clusters during the deposition. The background intensity for another substrate at 82 K was measured after helium gas was blown against the cooled substrate for 1 h under the same pressure conditions. The intensity from the adsorbed impurities is drawn with a thin line in Fig. 4(b). The pure diffraction intensity from gold clusters as given in Fig. 4(c) was obtained by subtracting the impurity component.

III. ANALYSIS

In this section we describe an analysis of the observed XRD pattern shown in Fig. 4(c). The conventional pattern-fitting procedures that have often been used to obtain the most adequate crystal structure cannot be easily used in the present case due to the existence of the size distribution. Furthermore, various analysis techniques commonly used in crystallography cannot be applied without modifications, because the structure of clusters is perfectly free from the translational and orientational symmetry rules. We, therefore, assumed several structure models, calculated XRD patterns taking the size distribution into consideration, and finally compared these with the observed pattern.

Four types of cluster structures; cuboctahedron, twinned cuboctahedron, icosahedron, and decahedron were assumed, where these models have exact geometrical structures. The closed-shell cluster models with different sizes are formed by

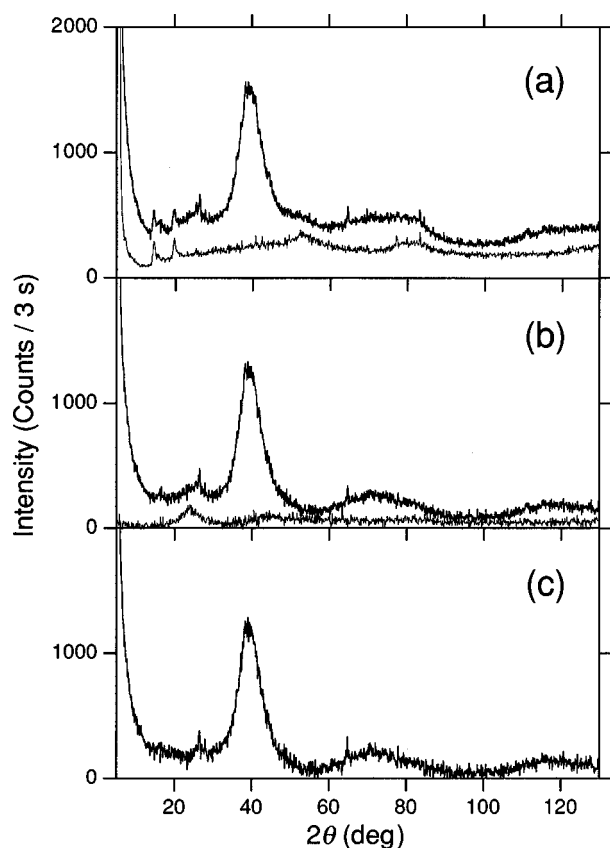


FIG. 4. (a) The thin line shows the background intensity from the Si substrate at 82 K before the deposition. The thick line shows the intensity measured *in situ* at 82 K after deposition of gold clusters on the cold substrate at 92 K for 1 h. (b) The thick line shows the difference of the two intensities shown in (a). This intensity is composed of signals from gold clusters and adsorbed impurity molecules. The thin line shows the contribution of impurity molecules that were adsorbed on another cold Si substrate while using only a helium gas stream under the same experimental conditions. (c) The diffraction intensity from gold clusters at 82 K, which was obtained by subtracting the impurity contribution.

building up a shell-wise sequence onto the smallest one. The numbers of atoms forming the first six closed shells are 13, 55, 147, 309, 561 and 923 for the cuboctahedron, the twinned cuboctahedron, and the icosahedron, and 7, 23, 54, 105, 181, and 287 for the decahedron. The twinned cuboctahedron introduced here has a (111) twin plane at the center of the cuboctahedron, which has been observed in some gold clusters with a diameter of 4 nm.²⁰ Although it has been found that some of them contained more than two parallel twin planes,²⁰ we have considered only the simplest case because the present cluster sizes were too small to introduce further twinning. A twinned cuboctahedron with three shells is built with a (111) stacking sequence of *ACBABCA*, while a regular cuboctahedron has *ABCABCA*.

The interatomic distance in gold crystals at 82 K was estimated approximately to be 0.288 nm derived from the interatomic distance at 293 K and the thermal expansion coefficient.²¹ This bulk value was used as the interatomic distance in the two model structures of the cuboctahedron and the twinned cuboctahedron. For the icosahedron and decahedron, we have employed the models proposed by Ino.^{22,23} The interatomic distances in both structures have

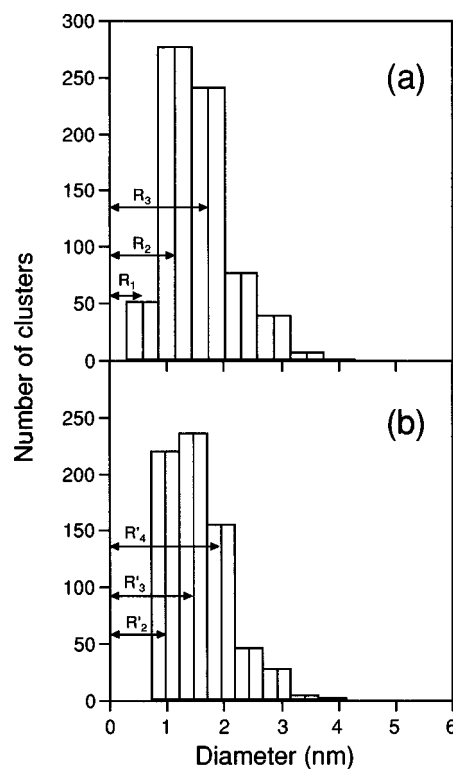


FIG. 5. (a) A size histogram for cuboctahedra and twinned cuboctahedra models with closed shells, which was obtained by reforming the size distribution shown in Fig. 2(a). R_n indicates the diameter of a model with n shells. (b) A size histogram for decahedra models with closed shells. R'_n indicates the apparent diameter of a decahedron with n shells viewed along the fivefold axis. The size histogram for icosahedra is similar to (a), therefore it is not shown here.

been given by a uniform elastic deformation of a unit tetrahedron using the elastic stiffness constants of gold crystals. The icosahedral structure has two different interatomic distances: the tangential distance is 2.75% longer and the radial distance is 2.28% shorter than the bulk one. In the decahedral model there are three different interatomic distances: the distance along the fivefold axis is 0.527% longer, the distance perpendicular to the fivefold axis is 1.09% longer, and the third distance is 0.396% shorter than the bulk one.

Since a large number of clusters were deposited on the cooled substrate with random orientation, the diffraction intensity can be described as an average of powder patterns from clusters with different sizes. To simulate a powder pattern that can be compared with the experimental one, the observed size distribution should be included into the calculation. The diameters of the cuboctahedral, the twinned cuboctahedral, and the icosahedral models with n shells are approximately $2n$ times the radial interatomic distance. We have reconstructed the size distribution with bins located at diameters of closed shells as shown in Fig. 5(a) for the cuboctahedral and the twinned cuboctahedral models. The reconstructed histogram for the icosahedral model was very similar to Fig. 5(a), therefore it is not shown here. The simulated diffraction intensity was produced by combining the intensity from each closed-shell structure using the reconstructed histogram as a weighting function. The way to reconstruct the size distribution for closed-shell decahedra dif-

fers from that for the above models. The HRTEM images of gold clusters show that all decahedra are located with their fivefold axis nearly perpendicular to the amorphous carbon surface. The histogram shown in Fig. 2(a), therefore, approximately shows the size distribution of the pentagons normal to the fivefold axis of the decahedron. A pentagon in the smallest decahedron is formed by five atoms with an interatomic distance which is 1.09% longer than the bulk one. The apparent diameter of this pentagon was regarded as twice the distance between a vertex and the center, i.e., 0.247 nm. The apparent diameter of the decahedron with n shells was considered to be $2n$ times this distance. The size distribution in Fig. 2(a) was reconstructed using bins located at the apparent diameters of closed-shell decahedra and yielded the histogram shown in Fig. 5(b); the simulated diffraction intensity for decahedra was then produced using this histogram as a weighting function.

The XRD intensity for a cluster model with n shells was calculated quantitatively on the basis of the kinematic theory from the following equation:

$$I_n(2\theta) = P(2\theta) \left(\sum_i \sum_j f_i(s) f_j(s) \frac{\sin(sr_{ij})}{sr_{ij}} \times \exp \left[-\frac{\delta_{ij}}{2} s^2 \right] + \sum_i S_i(s) \right), \quad (3)$$

where the first and second terms in the braces correspond to coherent and incoherent scatterings, respectively. In Eq. (3), $P(2\theta)$ is the polarization factor $[1 + \cos^2(2\theta_M)\cos^2(2\theta)]/[1 + \cos^2(2\theta_M)]$, $2\theta_M$ the (00-2) Bragg angle of the HOPG monochromator, s the scattering parameter $s = 4\pi \sin \theta/\lambda$, $f_i(s)$ the atomic scattering factor of atom i , r_{ij} the atomic distance between atom i and j , δ_{ij} mean-square deviation of the atomic distance r_{ij} due to thermal motions, and $S_i(s)$ the incoherent scattering function of atom i . We have neglected the δ_{ij} value in the following calculations, because the thermal motion of atoms is known to depend on the particle size⁹ and its value for small clusters is unknown. Calculations were done considering two characteristic x-ray lines, Cu $K\alpha_1$ and $K\alpha_2$, with an intensity ratio of 2 to 1. The calculated XRD intensities for four types of cluster models with 1–6 closed shells are shown in Figs. 6(a)–6(d). The XRD patterns from crystalline clusters such as twinned and non-twinned cuboctahedra showed broad peaks located at Bragg angles, which become sharper with increasing cluster size, while those from icosahedra and decahedra showed broad halos around the higher angle region even for larger cluster sizes. The simulated XRD patterns were derived using the following equation:

$$I_{\text{siml}}(2\theta) = \sum_n g_n I_n(2\theta), \quad (4)$$

where g_n is the reconstructed size histogram shown in Fig. 5(a) or 5(b), and $I_n(2\theta)$ is the calculated intensity from a cluster model with n shells according to Eq. (3). They are displayed in Figs. 7(a)–7(d). To enable a quantitative comparison between the experimental pattern and the simulated ones, the former has to be corrected with the absorption factor indicated by Eqs. (1) and (2), and with the instrumental

correction function as shown in Fig. 1. However there are still two unknown parameters: the mean thickness t and the mean density ρ of the cluster sample. Since both parameters have equal influence on the term $\zeta(2\theta, \rho t)$, we calculated its angular dependence for four different thicknesses, $t = 1, 10, 100, \text{ and } 1000 \text{ nm}$, using a fixed density value of the bulk gold, $\rho = 19.3 \text{ g/cm}^3$. All results showed a minimum at $2\theta = 92^\circ$ and a very small angular dependence for 2θ between 30° and 130° , which is the range where most of the signal from the gold clusters falls into. The difference between a minimum and a maximum never did exceed 4% even for the thinnest case, where the difference decreased with the thickness. Therefore, we assumed $\zeta(2\theta, \rho t)$ to be constant. The intensity curve finally obtained is shown in Fig. 7(e), and can be directly compared with the simulated ones.

IV. DISCUSSION

The simulated diffraction patterns from the crystalline cluster models, cuboctahedra, and twinned cuboctahedra, showed distinct Bragg peaks in the low angle region. The first three reflection lines, 111, 200, 220, can be easily assigned as shown in Figs. 7(a) and 7(b), even if the diffraction takes place in extremely small crystals. To the contrary, the noncrystalline models, icosahedra and decahedra, produced amorphouslike halo patterns as shown in Figs. 7(c) and 7(d). The experimental pattern in Fig. 7(e) resembles the simulated patterns of the noncrystalline models and is very different from those of the crystalline ones. Two simulated patterns of noncrystalline models show high similarity, since decahedral frames are shared in an icosahedron. However, regarding the shape of the first and third halos, the experimental pattern is more similar to the pattern from the decahedra model than to that from the icosahedral model. In the present HRTEM observations, icosahedral clusters could not be found, while we have often observed decahedral clusters. The present result of HRTEM observations well agreed with the x-ray result.

The HRTEM observations of gold clusters deposited sparsely on the amorphous carbon film at room temperature showed that the decahedral clusters oriented their fivefold axes with a few ten degrees from the substrate normal. Altenhein *et al.*²⁴ also observed the same feature in their room-temperature-deposited gold clusters. We discuss whether such a specially preferred orientation of decahedral clusters was also existent in the cold deposit. If all of the decahedral clusters were located with their fivefold axes parallel to the substrate normal, $\{110\}$ planes of each tetrahedral units would not contribute to the Bragg condition. There are six $\{110\}$ planes in one tetrahedral unit; one $\{110\}$ plane is perpendicular to the fivefold axis, another $\{110\}$ plane includes the fivefold axis, and the other four $\{110\}$ planes are at some special geometry. The first two $\{110\}$ planes cannot reflect the incident x rays due to the present grazing-incident geometry. The last four $\{110\}$ planes can put their normal axis on the scattering plane with $\theta \approx -60^\circ$ or $+60^\circ$, but these angles are far from the Bragg condition of 2θ for the Cu $K\alpha$ radiation. Therefore, such specially preferred orientations would drastically change the simulated powder pattern as shown in Fig. 7(d). The simulated intensity for such specially preferred orientations cannot be easily obtained due to the

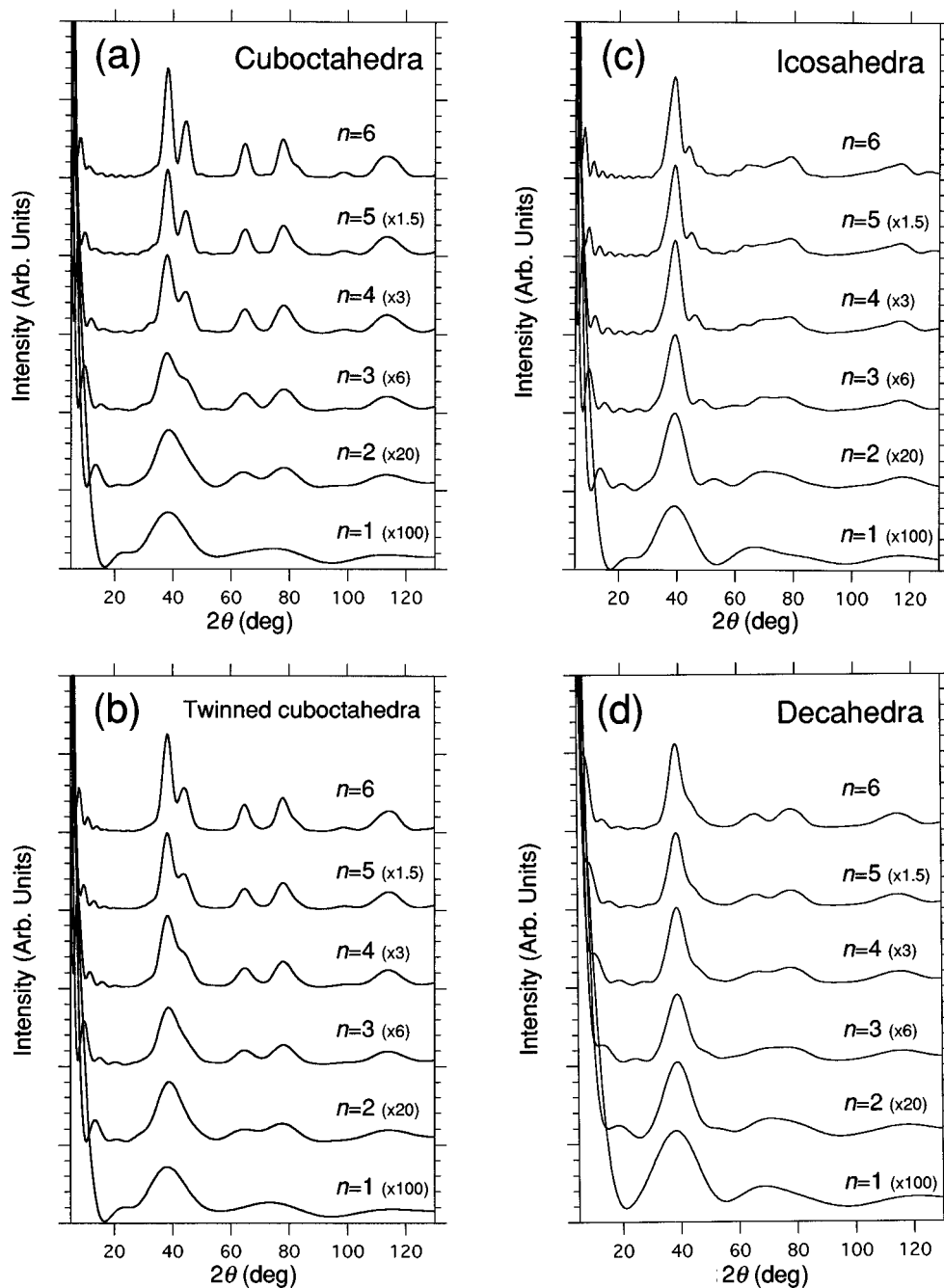


FIG. 6. Calculated diffraction intensities of closed shells of (a) cuboctahedra, (b) twinned cuboctahedra, (c) icosahedra, and (d) decahedra models. Each pattern is scaled into the highest one with proper magnification indicated in parentheses. The formula used for calculations given in Eq. (3).

unknown tilting angle distribution of the fivefold axis, however it would deviate largely from the powder pattern shown in Fig. 7(d) and would disagree with the experimental pattern. The origin that the decahedral clusters were deposited on the cooled substrate with random orientation is probably due to the presence of impurity molecules adsorbed simultaneously. At room temperature, it is natural that they lie down their flat bodies on the surface.

We further discuss some disagreement around the higher angle region between the simulated pattern of decahedral structures and the experimental one. The third halo of the experimental pattern in Fig. 7(e) seems to appear at a higher angle than that of the simulated one in Fig. 7(d). This indi-

cates that the interatomic distance in the gold clusters is shorter than in the bulk crystal. We have confirmed that the third peak position of the simulated pattern shown in Fig. 7(d) could be shifted toward that of the experimental one by reducing the bulk interatomic distance by a few percent. The reduction of the interatomic distance for gold clusters with the size of 1–3 nm has been observed to be 1–2.5% by using EXAFS.¹⁰ This agrees with our result qualitatively.

The second halo of the experimental pattern was broader than that of the simulated one for decahedra. One possible reason are some imperfections in the decahedral configuration. Many researchers have commonly observed inhomogeneous strains in decahedral multiply-twinned particles.^{25–27}

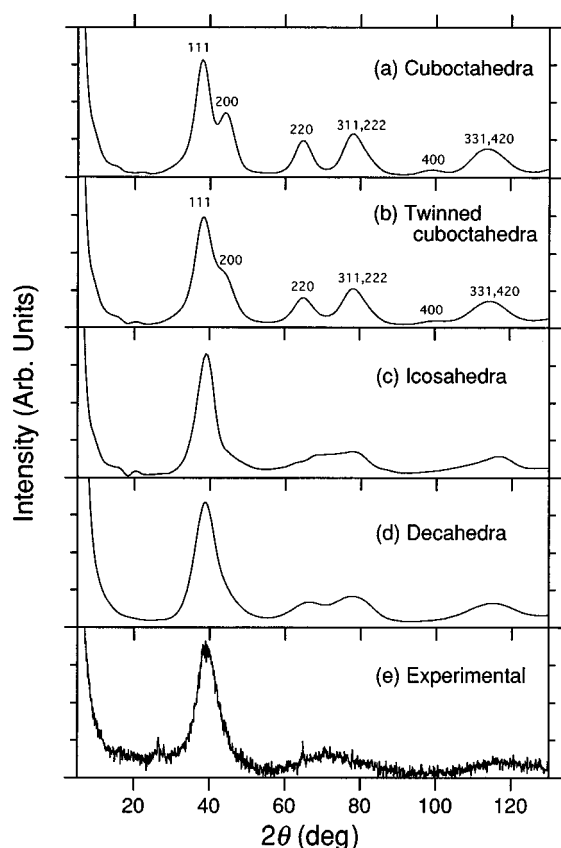


FIG. 7. Simulated diffraction patterns for (a) cuboctahedra, (b) twinned cuboctahedra, (c) icosahedra, and (d) decahedra models, which are produced by Eq. (4) using the calculated intensities for closed shells from Figs. 6(a)–6(d) and the histograms shown in Fig. 5(a) or 5(b). An experimental pattern corrected by the absorption and the instrumental factors is shown in (e).

A typical case is the presence of stacking faults running adjacent to, and parallel with, the twin boundaries.²⁸ Such non-uniform deformations reduce the strain energy in tetrahedral segments, however, compared with our case, they have been found in much larger particles (5–500 nm). In small particles (1–3 nm), it seems more plausible that homogeneous relaxation takes place. Because only one dislocation along one twin boundary can possibly displace all atoms in such a small system. The presence of inhomogeneous strains like a dislocation requires a minimum size of the particle. There are a few papers that pointed out the existence of imperfections of atomic positions along some twin boundaries in small decahedral gold particles.^{29,30} In our observations as shown in Figs. 3(a) and 3(b), it seems that five twin boundaries of these two clusters do not just join into one central point. However, it is difficult to prove the existence of inhomogeneous strains from these pictures, because the image can be drastically modified by even a small tilting angle of the fivefold axis according to the multislice calculations of TEM images for a gold decahedron.¹⁶ We have only considered the decahedral structure models with closed shells for the analysis of the x-ray-diffraction pattern. Open shell structures, however, should be also involved in the actual deposit. The existence of an incomplete decahedral layer probably produced an inhomogeneous deformation in the inside layers. This also might be one of the origins of the broader

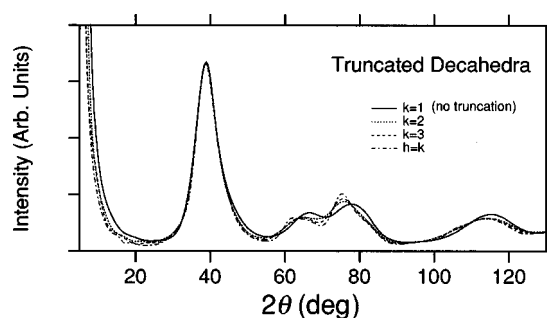


FIG. 8. Simulated diffraction patterns for truncated decahedra with different (100) truncation areas are represented by using h and k , where h is the number of atoms on the edge joining (100) and (111) faces and k is the number of atoms on the edge joining two (100) neighboring faces. The pattern for $k=1$ was simulated from nontruncated decahedra, which is the same as that shown in Fig. 7(d). The simulated patterns for $k=2$ and $k=3$ were obtained from models using these numbers for truncation. A pattern for $h=k$ was obtained from models with square (100) truncated planes.

second halo. We can therefore mention that our sample contained decahedral particles whose internal atomic positions were displaced from those in the ideal geometric models, since the present diffraction pattern provides the *average* information about various structural imperfections.

Regarding the previous theoretical works³¹ we also assumed other types of decahedral structures. These truncated decahedral structures are known as Ino's and Marks' decahedra, where the former is simply produced by truncating the five sides of decahedron with (100) planes and the latter is created by further facetting the five corners of the former with (111) planes. Several families with a different rectangular ratio of the (100) surface have been suggested.³¹ Facetting and truncation make the flat body more spherical and reduce the surface energy of the simple decahedral structure. Here we have simulated three kinds of diffraction patterns for Ino's decahedra with different truncation areas. The calculations were done following the same procedure as described above. The results are summarized in Fig. 8 and compared with the result for the regular decahedra ($k=1$) shown also in Fig. 7(d). The truncated (100) face was represented by using h and k , where h is the number of atoms on the edge joining (100) and (111) faces and k is the number of atoms on the edge joining two (100) neighboring faces. The first and second models had constant values of $k=2$ and $k=3$, respectively, and these numbers were kept independently of the model size. The third model has been constructed by keeping the relation of $h=k$, i.e., square (100) planes, which exhibited the most spherical form and probably the lowest-energetic structure in Ino's decahedral structures. However as the truncated area increased, modulation of the second halo became larger and gradually deviated from the experimental pattern shown in Fig. 7(e). Consequently, the area of the (100) truncated face, i.e., the k value, should be small or nonexistent, and decahedra with square (100) faces should not dominant in our sample. This result shows good agreement with the HRTEM results. Iijima and Ichihashi have observed a clear Marks' decahedron with 3 nm in diameter in fluctuating structures under the beam irradiation.¹⁷ Kizuka and co-workers have also found it in fluctuating structures.³² Such spherical decahedral structures

seem to appear as one of the stable structures by gaining thermal energy under the electron-beam irradiation, while the flat-body decahedral structure has been grown under non-equilibrium thermodynamic conditions in a gas phase and probably remained as a metastable form.

The present XRD results revealed that small gold clusters preferentially form decahedral structures under the present preparation conditions. In general, however, the cluster production tends to result in a uniform mixture of various sorts of structures.³³ The differences between the present result and the previous works are considered to be due to our unique production method. In our system, by changing the pressure difference between the two chambers, we can control the coalescence growth frequency in free space as described in our recent paper.³⁴ The large pressure difference and the geometry of the skimmer placed just above the center position of the crucible result in inhalation of the helium containing clusters grown from only vapor atoms emitted from the center. Under this specific condition the convective flow of helium is perfectly restrained and the laminar flow from under to over the crucible takes place effectively, and yielded the small average size of clusters with the fairly narrow size distribution. The fraction of the decahedral-type clusters was probably enhanced by picking up clusters formed homogeneously in the small central vapor region. The correlation between the production conditions and the resulting structures is, therefore, an important subject to be revealed.

About the growth sequence of decahedral clusters, we can speculate as follows. Under the present helium pressure condition, very rapid cooling of the vapor takes place, which leads to a homogeneous nucleation. The smallest decahedral clusters are initially created and survive well in the highly supersaturated vapor. They grow epitaxially by adsorbing vapor atoms onto their surface while keeping the decahedral shape, followed by the further coalescence growing. However, it is quite difficult to get a clear picture of how two decahedral clusters can produce a new similarly shaped cluster by coalescence. Nevertheless, it has been observed by an *in situ* TEM technique that a large decahedral particle coalesced with another small particle and grew into a new particle with a decahedral shape.³⁵ The coalescence event involves a neck formation followed by diffusion of surface atoms.^{36,37} During this diffusion, an epitaxial process seems to proceed, resulting in a new large decahedral particle. This can explain the previously observed fact that gigantic decahedral particles larger than 10 nm in diameter could often be grown through the gas-phase aggregation.³⁸

V. CONCLUSION

To identify what type of structure is the most probable for small gold clusters with 1–3 nm in diameter, we have performed both the HRTEM observation for the room-temperature isolated deposit and the *in situ* GIXRD measurement for the low-temperature-piled deposit. The HRTEM result showed that the decahedral multiply-twinned structures were frequently observed in clusters with 2–3 nm in diameter, however, the structural identification could hardly be accomplished for tiny clusters (1–2 nm) because of the dynamic structural fluctuation and the strong substrate images. But the observed GIXRD pattern could be analyzed quantitatively and compared with the simulated diffraction patterns from cuboctahedral, twinned-cuboctahedral, icosahedral, decahedral, and truncated-decahedral models with geometrical closed shells, which were calculated taking the observed size distribution into consideration. The observed pattern could not be explained by either of the crystalline cluster models, but agreed well with the simulated patterns from the decahedral model. The comprehensive conclusion considering both results is that the dominant structures of the small gold clusters prepared under our experimental conditions are decahedral structures with structural imperfections.

In this paper we have reported quantitative measurement and analysis of the x-ray Debye-Scherrer pattern from small gold clusters. The observed x-ray signals have mainly come from decahedral clusters having 3, 4, and 5 closed shells, and open shells inbetween, where the numbers of atoms constituting these closed shells are 54, 105, and 181, respectively. The present experiments have demonstrated that an extremely weak XRD signal from such a small cluster can be readily measured by preparing the cold cluster deposit using the LTCD technique. The XRD results were consistent with the HRTEM results, suggesting that the original structure in the gas phase survived even after quenching on the cold substrate. Since the x ray perturbs small clusters (1–2 nm) much less than the electron beam, they could retain the initial structure formed in the gas phase. From this point of view, the method, LTCD+GIXRD, offers possibilities to study the structure of clusters quantitatively and statistically. The present x-ray technique will be particularly useful for insulator clusters such as alkali halides and metal oxides, since for them HRTEM observation is usually difficult due to the electrical charge-up effect.

ACKNOWLEDGMENTS

The authors are grateful to Dr. J. Harada of Rigaku Co. Ltd. for his fruitful discussion and Professor O. Numata of University of Tsukuba for his permission to use TEM.

¹S. Ino, J. Phys. Soc. Jpn. **21**, 346 (1966).

²T. Komoda, Jpn. J. Appl. Phys. **7**, 27 (1968).

³A. Yokozeki and G. D. Stein, J. Appl. Phys. **49**, 2224 (1978).

⁴B. G. de Boer and G. D. Stein, Surf. Sci. **106**, 84 (1981).

⁵B. D. Hall, M. Flüeli, D. Reinhard, J.-P. Borel, and R. Monot, Rev. Sci. Instrum. **62**, 1481 (1991).

⁶L. S. Bartell, Chem. Rev. **86**, 491 (1986).

⁷A. Yokozeki, J. Chem. Phys. **68**, 3766 (1978).

⁸B. D. Hall, D. Reinhard, and D. Ugarte, Z. Phys. D **26**, S73

(1993).

⁹K. Ohshima and J. Harada, J. Phys. C **17**, 1607 (1984).

¹⁰A. Balerna, E. Bernieri, P. Picozzi, A. Reale, S. Santucci, E. Burattini, and S. Mobilio, Phys. Rev. B **31**, 5058 (1985).

¹¹P. A. Montano, H. Purdum, G. K. Shenoy, T. I. Morrison, and W. Schulze, Surf. Sci. **156**, 228 (1985).

¹²K. Koga and H. Takeo, Rev. Sci. Instrum. **67**, 4092 (1996).

¹³S. Yatsuya, S. Kasukabe, and R. Uyeda, Jpn. J. Appl. Phys. **12**, 1675 (1973).

- ¹⁴*International Tables for X-ray Crystallography*, edited by A. J. C. Wilson (Kluwer-Academic, The Netherlands, 1992), Vol. C, p. 502.
- ¹⁵C. G. Granqvist and R. A. Buhrman, *J. Appl. Phys.* **47**, 2200 (1976).
- ¹⁶J. Urban, H. Sack-Kongehl, and K. Weiss, *Z. Phys. D* **28**, 247 (1993).
- ¹⁷S. Iijima and T. Ichihashi, *Phys. Rev. Lett.* **56**, 616 (1986).
- ¹⁸P. M. Ajayan and L. D. Marks, *Phys. Rev. Lett.* **63**, 279 (1989).
- ¹⁹M. Mitome, Y. Tanishiro, and K. Takayanagi, *Z. Phys. D* **12**, 45 (1989).
- ²⁰S. Iijima, in *Proceedings of the XIth International Congress on Electron Microscopy*, edited by T. Imura, S. Maruse, and T. Suzuki (The Japanese Society of Electron Microscopy, Kyoto, 1986).
- ²¹*International Tables for X-ray Crystallography*, edited by C. H. Macgillavry and G. D. Rieck (Reidel, The Netherlands, 1983), Vol. III, p. 123.
- ²²S. Ino, *J. Phys. Soc. Jpn.* **26**, 1559 (1969).
- ²³S. Ino, *J. Phys. Soc. Jpn.* **27**, 941 (1969).
- ²⁴C. Altenhein, S. Giorgio, J. Urban, and K. Weiss, *Z. Phys. D* **19**, 303 (1991).
- ²⁵L. D. Marks, *Surf. Sci.* **150**, 302 (1985).
- ²⁶S. A. Nepijko, V. I. Styopkin, H. Hofmeister, and R. Scholtz, *J. Cryst. Growth* **76**, 501 (1986).
- ²⁷S. Iijima, *Jpn. J. Appl. Phys.* **26**, 357 (1987).
- ²⁸L. D. Marks and D. J. Smith, *J. Microsc.* **130**, 249 (1983).
- ²⁹P.-Y. Gao, W. Kunath, H. Gleiter, and K. Weiss, *Z. Phys. D* **12**, 119 (1989).
- ³⁰P. Gao, *Z. Phys. D* **15**, 175 (1990).
- ³¹C. L. Cleveland and U. Landman, *J. Chem. Phys.* **94**, 7376 (1991).
- ³²T. Kizuka, T. Kachi, and N. Tanaka, *Z. Phys. D* **26**, S58 (1993).
- ³³L. D. Marks, *Rep. Prog. Phys.* **57**, 603 (1994).
- ³⁴K. Koga, T. Ikeda, K. Ohshima, and H. Takeo, *Jpn. J. Appl. Phys.* **36**, 7050 (1997).
- ³⁵K. Yagi, K. Takayanagi, K. Kobayashi, and G. Honjo, *J. Cryst. Growth* **28**, 117 (1975).
- ³⁶S. Iijima and P. M. Ajayan, *J. Appl. Phys.* **70**, 5138 (1991).
- ³⁷W. Krakow, M. José-Yacamán, and J. L. Aragón, *Phys. Rev. B* **49**, 10 591 (1994).
- ³⁸L. D. Marks and D. J. Smith, *J. Cryst. Growth* **54**, 425 (1981).